symmetry

MDPI

Article

Effect of Silicon Addition on the Phase Symmetry and Microstructural Stability of High-Entropy Alloys During Heat Treatment

Sheetal Kumar Dewangan

Department of Materials Science and Engineering, Ajou University, Suwon 16499, Republic of Korea; sheetal@ajou.ac.kr; Tel.: +82-31-219-3422; Fax: +82-31-219-1613

Abstract

This study investigates the role of silicon (Si) addition in governing the evolution of phase symmetry and microstructural stability in a high-entropy alloy (HEA) synthesized via powder metallurgy. Mechanically alloyed powders were consolidated through conventional sintering, followed by systematic heat treatment to examine symmetry-driven phase transformations. Particular attention is given to the symmetry relationship between body-centered cubic (BCC) and face-centered cubic (FCC) crystal structures and their compositional stabilization mechanisms. X-ray diffraction and microstructural analyses reveal that Si incorporation modifies lattice symmetry, promotes controlled phase transformation, and influences the balance between competing crystallographic phases. The addition of Si contributes to symmetry stabilization by reducing heterogeneity in lattice distortion and suppressing grain coarsening during thermal exposure. These findings demonstrate that compositional tuning can regulate structural symmetry and phase equilibrium in multi-component alloy systems. The work provides insight into symmetry-controlled material design strategies for enhancing the thermal robustness and structural reliability of HEAs for high-temperature applications.

Keywords: mechanical alloying; Spark Plasma Sintering; high entropy alloy; phase symmetry

1. Introduction

The development of alloys has progressed continuously from ancient metallurgical practices to modern engineering materials, with each stage marked by significant technological advancements. Today, alloys constitute the backbone of numerous structural and functional applications because their properties can be tailored through careful control of composition and processing [1–3]. Among the conventional routes for alloy production, casting and powder metallurgy are the most widely used. Although casting is convenient and rapid, it often suffers from segregation, porosity, and non-uniform microstructures. Powder metallurgy, in contrast, has emerged as a highly effective approach for producing high-strength, compositionally uniform materials, particularly for complex, multi-component systems [4,5].

Alloy development has long been driven by the need to achieve a balanced combination of mechanical strength, thermal stability, corrosion resistance, and phase stability under service conditions [6,7]. Heat treatment is widely used to modify the microstructure and improve the properties of alloys [8,9]. Controlled thermal exposure can promote phase transformation, relieve internal stresses, and enhance elemental homogeneity. As a result,

Check for updates

Academic Editors: Noé Cheung, André Barros and Felipe Bertelli

Received: 26 February 2026
Revised: 26 March 2026
Accepted: 27 March 2026
Published: 30 March 2026

Copyright: © 2026 by the author. Licensee MDPI, Basel, Switzerland. This article is an open access article distributed under the terms and conditions of the Creative Commons Attribution (CC BY) license.

key properties such as hardness, strength, and thermal stability are significantly affected. Understanding the relationship between heat treatment and resulting material properties is essential for optimizing alloy performance in advanced engineering applications. Conventional alloy systems such as aluminum alloys, nickel-based superalloys, titanium alloys, and Fe-based steels rely on controlled alloying additions and heat-treatment routes to tailor phase constitution and microstructural symmetry, thereby optimizing performance for targeted applications [1,10–12]. Traditional metallurgical understanding suggested that combining several principal elements would inevitably lead to the formation of multiple intermetallic compounds and intricate microstructures. In recent years, high-entropy alloys (HEAs), characterized by their multi-principal element compositions, have attracted significant attention due to their high configurational entropy, sluggish diffusion, and enhanced thermal stability compared to traditional alloys [13–16]. Numerous studies have reported that minor elemental additions can strongly influence phase symmetry (FCC, BCC, or dual-phase), lattice distortion, precipitation behavior, and grain stability during thermal exposure. In particular, metalloid and light-element additions, such as Al, Si, and B, have been shown to modify bonding characteristics, stabilize specific crystal structures, and improve high-temperature strength and oxidation resistance in both conventional alloys and HEAs [17,18]. Silicon, widely used in steels, Al-based alloys, and Ni-based superalloys for its role in solid-solution strengthening, oxidation resistance, and phase stabilization, has recently emerged as an effective tuning element in HEAs, where it can alter phase symmetry and suppress microstructural degradation during heat treatment [19,20]. These findings highlight the importance of systematic investigations into the role of silicon in governing the phase evolution and microstructural stability of HEAs under thermal processing conditions. In addition, machine learning has emerged as a powerful tool in alloy development by enabling data-driven exploration of complex composition-processing-microstructure-property relationships, thereby accelerating materials discovery and reducing experimental trial-and-error [21–24].

However, advances in mechanical alloying (MA) and the concept of high-entropy alloys (HEAs) have transformed this perception. MA, a solid-state powder-processing technique, enables atomic-scale mixing and facilitates the formation of metastable, nanocrystalline, or even single-phase solid solutions [25,26]. Sequencing strategies during mechanical alloying have demonstrated a crucial impact on phase stabilization. For example, Vaidhya et al. showed that controlled sequential addition of elements in AlCoCrFeNi HEAs can significantly influence the final phase constitution: a pure BCC phase emerged for the sequence AlNi + Co + Fe + Cr, whereas FeNi + Co + Cr + Al produced a dual BCC–FCC structure [27,28]. Despite its many advantages, MA is not free of challenges; contamination from milling media and process control agents remains a concern, though it can be minimized through careful material selection, inert-gas atmospheres, and shorter milling durations.

Within this framework, Al-Fe-Co-Ni-based HEAs have gained considerable interest due to their promising combination of strength, thermal stability, and relatively low density [29–31]. The incorporation of silicon into this alloy system further enhances configurational entropy, influences lattice distortion, and improves mechanical performance. High-energy ball milling efficiently synthesizes $AlFeCoNiSi_x$ (x = 0, 0.4, 0.8) alloys via solid-state diffusion and homogeneous mixing, while conventional sintering subsequently densifies the material without compromising the refined microstructure. Post-sintering heat treatments play an essential role in modulating phase evolution, chemical ordering, and lattice relaxation.

X-ray diffraction (XRD) serves as a powerful tool for monitoring these structural transformations. Symmetry analysis of XRD patterns, including peak positions, intensities,

broadening, and reflections unique to specific crystal structures, provides deep insights into how Si addition and processing conditions influence the alloy system. In $AlFeCoNiSi_x$ alloys, changes in symmetry can reveal the transition between BCC, FCC, ordered B2 phases, or multiphase configurations, as well as lattice distortion effects arising from element substitution and thermal treatment. Therefore, the present study integrates mechanical alloying, conventional sintering, and subsequent heat treatment to investigate the structural evolution and symmetry changes in AlFeCoNiSi high-entropy alloys. Through a comprehensive analysis of XRD patterns, this work aims to elucidate the impact of Si addition on phase formation pathways and the thermodynamic and kinetic mechanisms governing symmetry transitions in these multi-component alloy systems.

2. Materials and Methods

High-purity metal powders (>99.5%, Alfa Aesar, Ward Hill, MA, USA) were employed to synthesize the $AlFeCoNiSi_x$ (x = 0, 0.4, 0.8) high-entropy alloy system. The elemental powders were initially subjected to mechanical alloying in a high-energy planetary ball mill (Retsch PM-400 MA, Haan, Germany), with a milling speed of 300 rpm under ambient laboratory conditions for 10 h. Stearic acid was introduced as a process control agent, and 20 mm steel balls were used as the milling media. The ball-to-powder ratio (BPR) was maintained at 10:1 throughout the milling operation.

Phase evolution in the mechanically alloyed powders was examined by X-ray diffraction (XRD) using a Rigaku diffractometer equipped with a Cu Kα radiation source. The measurements were conducted at an operating voltage of 40 kV and a current of 40 mA. Diffraction patterns were collected over a 2θ range of 30–80°, with a step size of 0.02° and a scanning rate of 0.5°/min. Microstructural features of the milled powders were further characterized using a field-emission scanning electron microscope (FE-SEM, JSM-7500F, JEOL, Tokyo, Japan).

Pellet compaction was carried out using a hydraulic press at 20 MPa with a holding time of 1 min. The green compacts were subsequently sintered in a vacuum furnace under an argon atmosphere at 700 °C for 1 h. For a better conversation, the sintered sample is nominated as 0 Si, 0.4 Si, and 0.8 Si to $AlFeCoNiSi_x$ (x = 0, 0.4, 0.8), respectively. Additional heat-treatment cycles were performed at 800 °C to study the thermal stability and phase evolution of the alloy system. Post-treatment characterization included repeat XRD analysis and SEM imaging, along with elemental composition verification via energy-dispersive spectroscopy (EDS).

3. Thermodynamic Parameters for Solid Solution Formation

Phase formation in high-entropy alloys (HEAs) is primarily controlled by the interplay between enthalpy (ΔH_{mix}) and entropy (ΔS_{mix}) in the Gibbs free energy (ΔG_{mix}). A negative ΔG_{mix} favours thermodynamic stability and dictates whether a solid solution, intermetallic, or multiphase structure forms. The Ω parameter quantifies the balance between ΔH_{mix} and ΔS_{mix}. High Ω values indicate entropy dominance, promoting stable solid solutions, while low Ω values Favor ordered or intermetallic phases. Increased configurational entropy (ΔS_{mix}), following Boltzmann's hypothesis, enhances single-phase formation, especially at elevated temperatures. The alloy's weighted average melting temperature (Tm) influences Ω and thermal stability, while atomic size difference (δ) measures lattice distortion; larger δ values can induce strain, destabilize solid solutions, or favour amorphous/multiphase structures. Finally, the valence electron concentration (VEC) empirically predicts phase type: high VEC stabilizes FCC structures, low VEC favours BCC, and intermediate VEC values often yield mixed FCC + BCC microstructures.

The thermodynamic parameters listed in the table (Table 1) offer a quantitative basis for understanding phase stability and structural changes in high-entropy alloys (HEAs). The interaction between the enthalpy of mixing (ΔHmix) and the entropy of mixing (ΔSmix) shapes the Gibbs free energy landscape and, as a result, determines whether the alloy forms a solid solution or intermetallic compounds. A moderately negative ΔHmix encourages atomic bonding without strongly favouring the formation of ordered compounds, while a sufficiently high ΔSmix resulting from the randomness of multi-element configurations stabilizes disordered solid-solution phases. The calculated Ω parameter further illustrates this balance; higher Ω values signify stronger entropy-driven stabilization, suggesting a higher chance of forming a single-phase solution, especially at elevated temperatures. Likewise, the weighted melting temperature (Tm) affects the entropy contribution via the Ω ratio and aids in predicting the alloy's thermal stability during sintering and heat treatment [32].

Table 1. Thermodynamic relations and their description.

Thermodynamic Relations	Description
$\Delta H_{mix} = \sum_{i=1}^{n} \Omega_{i,j} c_i c_j$	Here ΔH_{mix} is the enthalpy of mixing of binary alloys, and Ω_{ij} ($\Omega_{ij} = 4\Delta H_{mix}^{AB}$) is a parameter for the regular melt interaction between the ith and jth elements
$\Delta S_{mix} = -R \sum_{i=1, i \neq j}^{n} (c_i \ln c_i)$	Where C_i is the molar percent of the mixing elements, and R is the gas constant with the value 8.314 JK^{-1} mol^{-1}. The following relation can calculate the melting temperature Tm of the n-element alloy
$T_m = \sum_{i=1}^{n} c_i (T_m)_i$	$(T_m)_i$ is the melting point of the ith component alloy
$\delta = 100 \sqrt{\sum_{i=1}^{n} c_{i=1} c_i (1 - \frac{r_i}{\bar{r}})^2}$	The atomic size difference (δ) is the important parameter for the phase formation, which is described through, and $\bar{r}$ is the average atomic radius of the alloying elements that can be calculated by the relation $\bar{r} = \sum_{i=1}^{n} c_i r_i$
$VEC = \sum_{i=1}^{n} c_i (VEC)_i$	The formation of the BCC or FCC depends on the VEC (Valence Electron Concentration); the quantitative prediction of the structure of the BCC or FCC in n-element alloys, as mentioned by Guo [33]. The relation between the VEC and the concentration of the n component elements is given in Equation.

Complementing these thermodynamic indicators, the atomic size difference (δ) and the valence electron concentration (VEC) provide additional insights into structural tendencies. The δ parameter captures lattice distortion arising from atomic radius mismatch; when δ is moderate, solid-solution formation is favoured, whereas large δ values lead to significant lattice strain, promoting multiphase or amorphous structures. Meanwhile, VEC serves as an empirical guide for predicting the crystal structure: higher VEC values favour FCC stability, lower values support BCC formation, and intermediate values yield mixed-phase configurations. Together, these thermodynamic and electronic parameters establish a coherent framework for interpreting the observed phase evolution in AlFeCoNi upon adding Si to the system. The calculated properties have been given in Table 2.

Table 2. Physiochemical and thermal properties of the $AlFeCoNiSi_x$ system.

Alloys	ΔH_{mix} (KJ/mol)	ΔS_{mix} (JK^{-1} mol^{-1})	T_m (°C)	δ (%)	VEC
$AlFeCoNiSi_0$	−12.8	1.39 R	1287	10.5	7.5
$AlFeCoNiSi_{0.4}$	−21.3	1.58 R	1296.1	12.5	7.23
$AlFeCoNiSi_{0.8}$	−27.2	1.61 R	1308.2	13.3	6.92

4. Result and Discussion

4.1. Morphology and Phase Evolution of Ball-Milled HEA Powder

The SEM images in Figure 1a–c show the morphology of the $AlFeCoNiSi_x$ (x = 0, 0.4, 0.8) powders before mechanical milling. The particles appear coarse, angular, and structurally heterogeneous, reflecting the intrinsic morphology of the as-received elemental powders. Large, irregular fragments co-exist with smaller particles, indicating poor size uniformity and limited intermixing among the constituents. The presence of sharp edges and relatively smooth surfaces suggests that the powders retain their original metallic characteristics, with minimal plastic deformation or fragmentation at this stage.

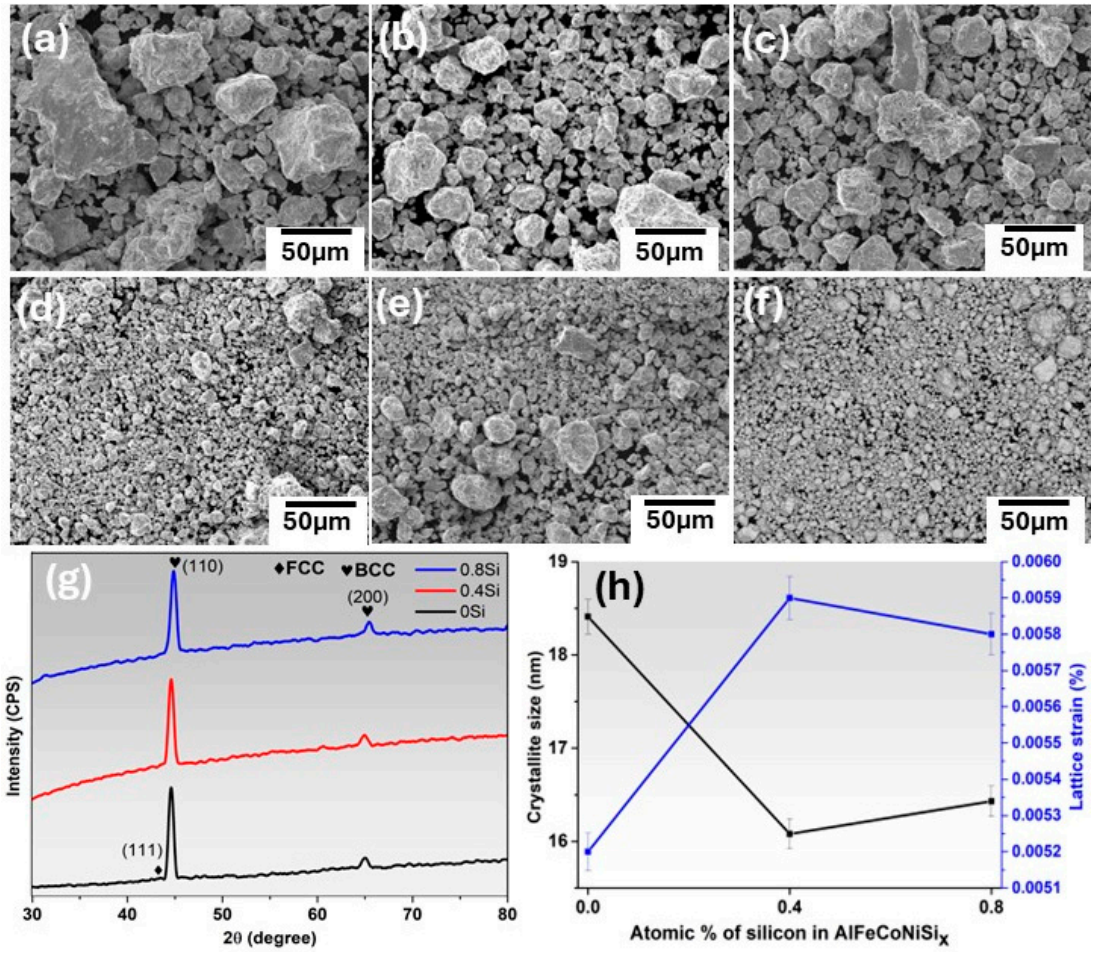


Figure 1. Initial alloy powders (**a**–**c**), and 10 h milled powder (**d**–**f**) of 0 Si, 0.4 Si, 0.8 Si alloys, (**g**) XRD pattern of alloys after the milling, and (**h**) crystallite size vs. lattice strain plot with respect to Si variation.

In contrast, the micrographs in Figure 1d–f reveal the morphological evolution after 10 h of high-energy ball milling. The powders exhibit a significantly refined and homogenized microstructure, characterized by irregular but much smaller particle sizes. The

repeated fracturing and cold-welding events during milling lead to substantial plastic deformation, resulting in a dense population of ultrafine particles and the disappearance of the large primary fragments observed earlier. The increased surface roughness and more uniform particle-size distribution indicate effective alloying among the constituent elements, reflecting the mechanical alloying process's solid-state diffusion and structural refinement.

The XRD patterns in Figure 1g present the phase evolution of the milled $AlFeCoNiSi_x$ powders with varying Si content (0 Si, 0.4 Si, and 0.8 Si). All compositions exhibit dominant diffraction peaks corresponding to a BCC solid-solution phase, particularly the (110) and (220) reflections. The presence of only BCC peaks confirms that mechanical alloying successfully promotes extensive elemental mixing, enabling the formation of a single-phase structure even without subsequent sintering or heat treatment.

A noticeable trend is the peak shift and broadening with increasing Si content. The gradual shift of the (110) and (220) peaks toward higher angles for higher Si fractions indicates a reduction in lattice parameter, consistent with the incorporation of smaller Si atoms into the BCC lattice. Peak broadening further suggests reduced crystallite size and increased lattice strain, both characteristic effects of mechanical alloying and enhanced by the addition of Si. Moreover, the relative intensity variation of the peaks across compositions may reflect changes in preferred orientation or micro-strain distribution induced by Si substitution [34]. In addition, the elemental distribution analysis was carried out to evaluate the homogeneity of the alloy system, as shown in Figure 2a–c. The results indicate that all constituent elements are uniformly distributed throughout the HEAs, confirming effective mixing during the mechanical alloying process. Furthermore, the added Si is also found to be evenly dispersed within the alloy matrix, suggesting successful incorporation without noticeable segregation.

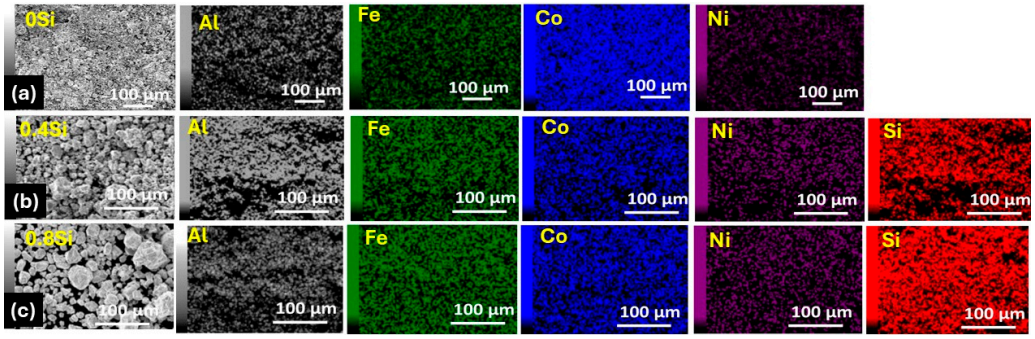


Figure 2. SEM-elemental distribution of the alloys (**a**) 0 Si, (**b**) 0.4 Si, and (**c**) 0.8 Si.

4.2. Phase Evaluation and Morphology of Sintered HEA Powder After Compaction

The conventionally sintered pellets of $AlFeCoNiSi_x$ (x = 0, 0.4, 0.8), shown in Figure 3a–c, exhibit uniform cylindrical geometry with visibly smooth surfaces, indicating successful compaction and densification during the sintering process. Additionally, to understand the characteristics of the alloy powder, particle size was calculated and presented in Figure 3d. The pellets maintain consistent dimensions across all compositions, suggesting that the powder flowability and compressibility were not adversely affected by Si addition. A slight variation in surface tone can be observed, particularly for the higher Si content, which may be attributed to differences in oxide formation, surface diffusion behavior, or sintering kinetics influenced by Si. The complete structural integrity of all pellets reflects effective consolidation at the selected sintering temperature, enabling the formation of mechanically stable bulk specimens suitable for subsequent microstructural and phase analysis [35].

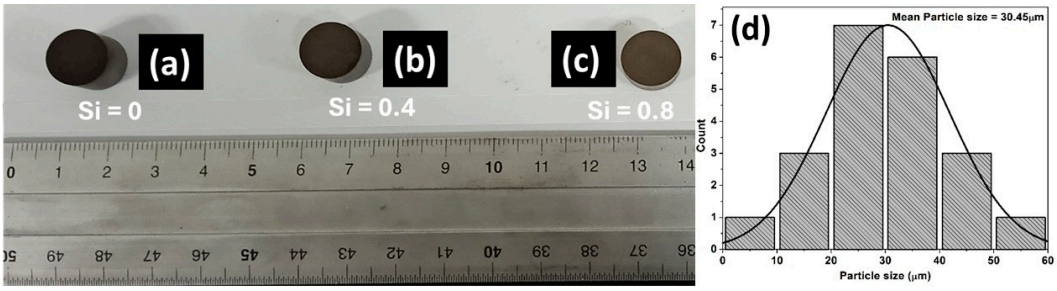


Figure 3. Compressed and sintered pallets of (**a**) 0 Si, (**b**) 0.4 Si, and (**c**) 0.8 Si alloys and (**d**) a histogram to present the particle size distribution of the alloyed powder.

The SEM micrographs of the sintered AlFeCoNiSi$_x$ alloys (Figure 4a–c) reveal significant microstructural evolution compared with the mechanically alloyed powders. After sintering at 700 °C, the particle boundaries appear smoother, and partial neck formation is evident, indicating the onset of solid-state diffusion and consolidation. In the 0 Si sample (Figure 1a), relatively larger and loosely bonded agglomerates can be observed, suggesting limited densification at this temperature. With the addition of Si (Figure 1b,c), the microstructure becomes progressively refined and more compact. The powders display enhanced particle bonding and reduced interparticle porosity, which suggests that Si promotes improved diffusion and assists in the formation of more homogeneous microstructural features. The finer features in the higher-Si alloy indicate that Si addition contributes to lattice distortion and diffusion-driven microstructural refinement during sintering.

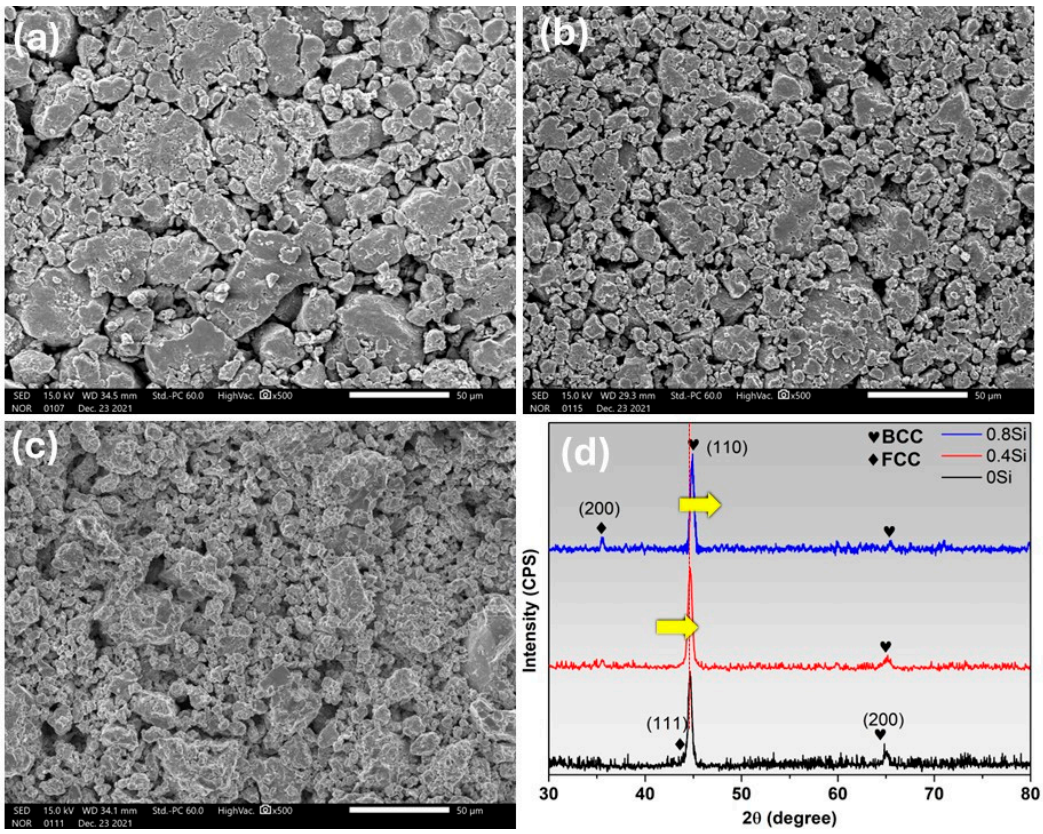


Figure 4. SEM morphology of sintered pallets of (**a**) 0 Si, (**b**) 0.4 Si, (**c**) 0.8 Si alloys and (**d**) XRD pattern of alloys after sintering at 700 °C as shifting of peaks.

The XRD patterns in Figure 4d provide insights into the phase evolution of the sintered HEAs. All compositions retain the dominant BCC solid-solution phase (Im-3m), as

evidenced by the (110) and (200) reflections. However, the Si-free alloy exhibits additional weak peaks corresponding to an FCC phase, suggesting incomplete homogenization or the persistence of metastable elemental clusters. As Si content increases to 0.4 and 0.8, only BCC peaks are observed, indicating that Si addition favours the stabilization of a single BCC phase at the sintering temperature. This stabilization may be attributed to enhanced configurational entropy and atomic size mismatch introduced by Si, which suppresses the formation of ordered intermetallics or secondary phases. Peak broadening in the higher Si alloys further suggests increased macrostrain and lattice distortion, consistent with the SEM observations of finer microstructural features and improved elemental mixing.

In addition to configurational entropy and lattice distortion effects, the role of Si can be better understood from a metallurgical perspective. Si is known to act as a ferrite (BCC) stabilizer, particularly in Fe-based alloy systems, by reducing the valence electron concentration (VEC, which is reduced from 7.5 to 6.92), which favours the formation of BCC over FCC structures. Furthermore, Si influences the electronic structure and bonding characteristics, promoting directional bonding that stabilizes the BCC lattice. During heat treatment, enhanced atomic diffusion facilitates the redistribution of elements, and the presence of Si energetically favours the transformation of any metastable FCC phase into a more stable BCC phase. Thus, the observed FCC-to-BCC transition is driven by a combination of thermodynamic stability (VEC effect) and diffusion-assisted phase evolution, rather than configurational entropy alone.

The SEM images reveal significant microstructural evolution in the samples subjected to 800 °C heat treatment. In Figure 5a, the microstructure appears relatively dense, with particles showing partial sintering and neck formation. The grains are closely packed, and the reduction in surface asperities suggests the onset of solid-state diffusion at this temperature. Minimal porosity is visible, indicating improved particle cohesion. In contrast, Figure 5b displays a more pronounced sintering effect, with larger, well-defined grains separated by interconnected pore channels. The increased pore visibility suggests that the sample composition or silicon content influences the sintering behaviour. Larger grains indicate enhanced diffusion and localized grain growth, which often occurs when elemental additions modify the diffusion kinetics or inhibit densification.

Figure 5c presents an even more heterogeneous microstructure, characterized by a combination of large, irregular grains and surrounding finer particles. The higher number of fine dispersed phases between larger grains suggests incomplete densification and inhibited grain coalescence, possibly due to silicon alloying. Silicon is known to affect wetting behavior and diffusion pathways; hence, increasing Si content may disrupt uniform grain growth and retain finer phases within the matrix. Overall, the SEM analysis suggests that heat treatment at 800 °C promotes sintering and grain formation, but silicon influences the degree of densification and microstructural uniformity.

The XRD profiles in Figure 5d show distinct phase transformations driven by the 800 °C heat treatment and varying silicon content. For the base composition (0 Si), the diffraction peaks correspond primarily to the FCC structure, indicating that the matrix retains its original phase after heat exposure. However, with the introduction of Si (0.4 Si and 0.8 Si), there is a noticeable emergence and strengthening of BCC-phase peaks, marked by the corresponding symbols in the diffractogram.

The progressive intensification of BCC peaks with increasing Si content indicates that silicon promotes the stabilization or formation of a BCC solid-solution phase at elevated temperature. This phase transformation is typical in refractory or Fe-based systems where silicon acts as a ferrite stabilizer. At higher Si concentrations (0.8 Si), the BCC peaks become dominant, confirming that silicon significantly alters the thermodynamic stability of the phases. The shift from FCC to BCC structure implies enhanced thermal stability, reduced

lattice distortion, and modified mechanical behavior, particularly at high temperatures. Additionally, the relatively sharper peaks in Si-containing samples suggest improved crystallinity after the 800 °C treatment. The suppression of FCC peaks with increasing Si further demonstrates competitive phase formation, where the BCC phase becomes energetically more favorable under these thermal conditions.

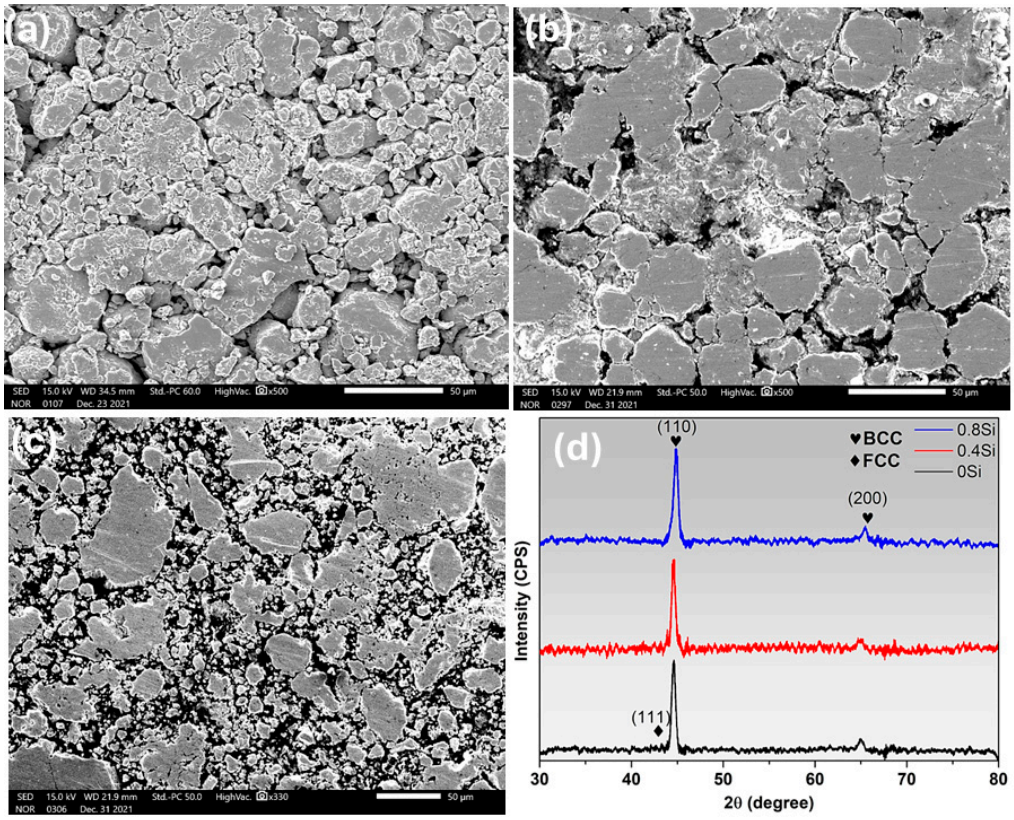


Figure 5. SEM morphology of sintered pallets of (**a**) 0 Si, (**b**) 0.4 Si, (**c**) 0.8 Si alloys, and (**d**) XRD pattern of alloys after sintering at 800 °C.

4.3. Discussion on Symmetry, Peak Shifting, and Heat-Treatment Effects

The XRD patterns in Figure 6a show a noticeable shift in the main diffraction peaks after sintering and subsequent heat treatment, reflecting significant changes in lattice symmetry and phase stability. In the as-milled powders, the peaks correspond predominantly to the BCC structure for the 0 Si alloy (Figure 1g). The dominant diffraction peak at $2\theta \approx 44.4°$ ($d \approx 2.037$ Å) corresponds to the BCC (110) reflection; indexing gives a lattice parameter $a \approx 2.88$, consistent with a BCC Im-3m matrix. In contrast, Si-containing alloys exhibit a broadened and slightly shifted profile due to the coexistence of FCC and emerging BCC symmetry. After sintering, however, the main peak moves toward higher 2θ values for all compositions, indicating lattice contraction caused by stress relaxation and partial homogenization [31]. This behavior aligns with the crystallite size and lattice strain values in the table: the sintered state shows reduced lattice strain (e.g., $AlFeCoNiSi_0$ from 0.0052 to 0.0023), which causes sharpening and more pronounced symmetry of the dominant FCC or BCC peaks. The thermal treatment at 700–800 °C further alters the peak positions, with the appearance of more prominent BCC peaks in Si-containing alloys. This shift confirms that silicon promotes the stabilization of BCC symmetry at elevated temperatures, consistent with the increased crystallite size (22–26 nm) and reduced lattice strain observed after 800 °C heat treatment, as shown in Table 3.

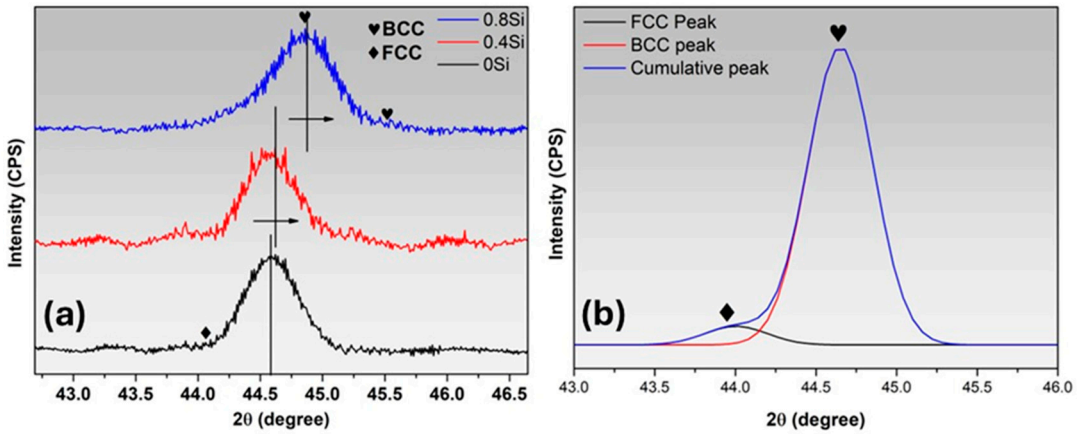


Figure 6. XRD patterns of HEAs (**a**) a noticeable shift in the main diffraction peaks after addition of Si element, (**b**) the coexistence of dual phases within the alloy.

Table 3. Effect on crystallite size and lattice strain after different processes.

Alloys	Powder		As Sintered at 700 °C		Heat Treatment at 800 °C	
	Crystallite Size (nm)	Lattice Strain	Crystallite Size (nm)	Lattice Strain	Crystallite Size (nm)	Lattice Strain
$AlFeCoNiSi_0$	18.41	0.0052	40.76	0.0023	14.70	0.0065
$AlFeCoNiSi_{0.4}$	16.08	0.0059	13	0.0073	22.41	0.0043
$AlFeCoNiSi_{0.8}$	16.43	0.0058	0.0028	0.0065	26.02	0.0037

The peak overlap illustrated in Figure 6b further supports the coexistence of dual phases and highlights the complexity of symmetry evolution during heat treatment. The FCC peak, positioned at a slightly lower 2θ value, merges with the emerging BCC peak at higher 2θ as Si content increases [32]. This overlap indicates that both phases contribute to the cumulative peak profile, resulting in a broader, asymmetric peak. For further understanding of the phase evaluation, Rietveld refinement has been performed on the XRD patterns to quantitatively evaluate the phase fractions, and result has been presented in Figure 7a–c. The analysis reveals that the Si-free alloy contains both BCC (~85%) and a minor FCC (~15%) phase. With the addition of Si, the FCC phase is completely suppressed, and the alloy exhibits a fully BCC structure (100%), as confirmed for higher Si contents.

In addition to this, the effect of the heat treatment has been investigated on bulk samples to understand the density. The results show (Figure 7d) that, although the theoretical density decreases with increasing Si content, the relative density exhibits a clear increasing trend, particularly for the 0.8 Si alloy. This indicates improved densification and reduced porosity with Si addition. The enhancement in relative density is consistent with the observed microstructural features, such as improved particle bonding and reduced pore fraction, confirming that Si promotes more effective sintering.

Such behavior is typical of multi-phase high-entropy alloys, where elements with different atomic sizes and diffusion rates produce simultaneous strain relaxation and structural reorganization during annealing. The table supports this interpretation: after heating to 800 °C, the 0 Si alloy shows reduced crystallite size and increased lattice strain, evidence of partial recrystallization, whereas Si-alloyed compositions show increased crystallite size and reduced strain, indicating enhanced structural ordering. Thus, the heat treatment not only sharpens and shifts the primary peaks but also strengthens the BCC phase fraction, leading to clearer symmetry separation in high-Si compositions and pronounced peak overlap in low-Si ones.

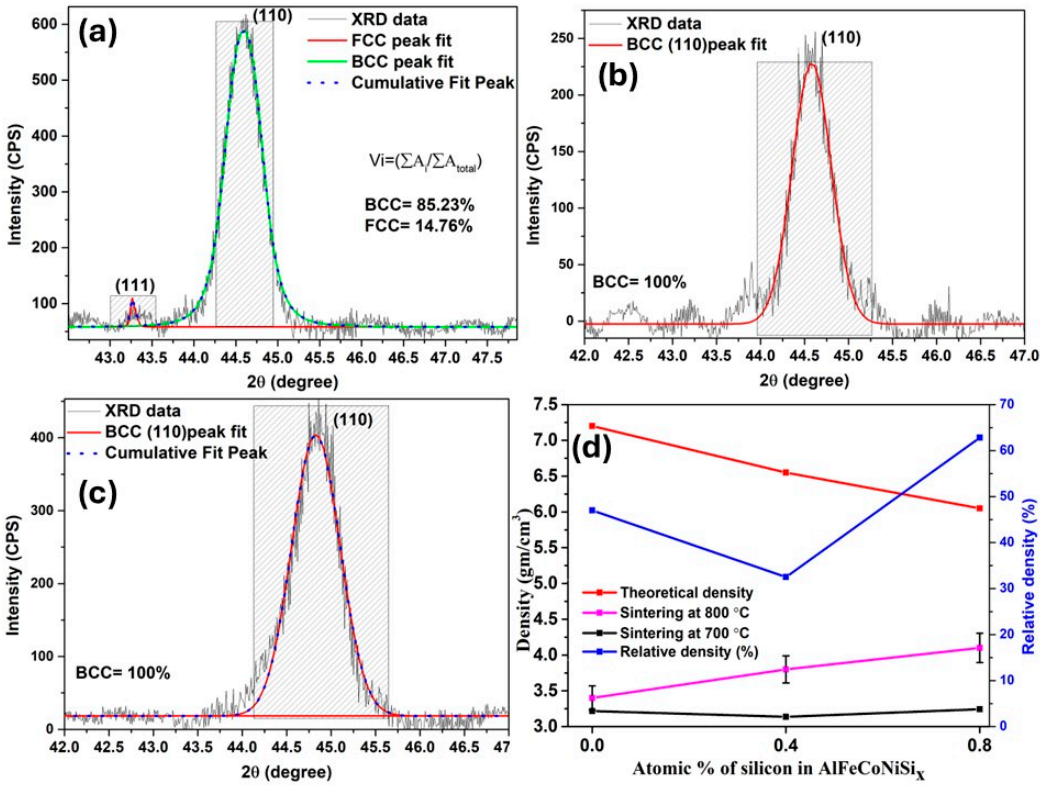


Figure 7. Rietveld analysis for phase quantification of (**a**) 0 Si, (**b**) 0.4 Si, (**c**) 0.8 Si alloys, and (**d**) Variation of theoretical density, experimental density (sintered at 700 °C and 800 °C), and relative density as a function of Si content.

A representation of symmetry evolution which is reflected in XRD peak profiles before and after heat treatment as shown in Figure 8. The as-sintered alloy exhibits broadened and asymmetric diffraction peaks due to lattice strain and small crystallite size, while heat treatment at 800 °C results in sharper, more symmetric peaks, indicating reduced lattice strain, improved crystallite ordering, and enhanced structural symmetry promoted by silicon addition.

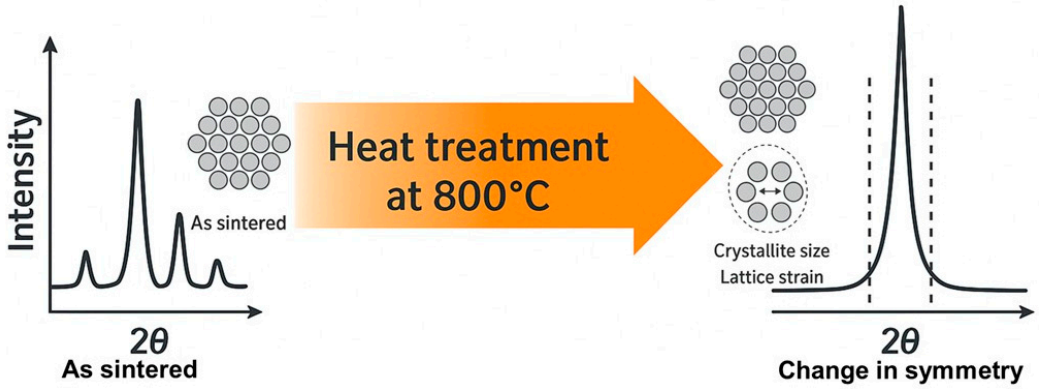


Figure 8. Illustrative XRD peak evolution showing symmetry modification with silicon addition and heat treatment.

5. Conclusions

In this study, AlFeCoNiSi$_x$ (x = 0, 0.4, 0.8) high-entropy alloys were synthesized via mechanical alloying followed by sintering at 700 °C to investigate the effect of Si on microstructure and phase stability. The sintered alloys showed improved densification and particle bonding with increasing Si content, evidenced by smoother interfaces, reduced

porosity, and finer morphology. XRD results confirmed a predominantly BCC structure for all compositions, while the Si-free alloy exhibited minor FCC phases. The disappearance of FCC peaks and sharpening of BCC reflections with increasing Si indicate that Si effectively stabilizes the single BCC phase.

Additionally, crystallite size and lattice strain analysis reveal that Si suppresses excessive grain growth and maintains lattice distortion during sintering, while heat treatment at 800 °C promotes strain relaxation and improved structural ordering in Si-containing alloys. In contrast, the Si-free alloy shows increased strain and reduced stability after heat treatment. In summary, Si addition stabilizes the BCC symmetry by maintaining controlled lattice distortion during sintering and enabling effective strain relaxation upon heat treatment, thereby suppressing secondary phases and improving microstructural uniformity in $AlFeCoNiSi_x$ high-entropy alloys.

Funding: This research received no external funding.

Data Availability Statement: The datasets generated and analyzed during the current study are available within the article. No additional data are required to support the findings of this study.

Acknowledgments: This research was supported by the Basic Science Research Program through the National Research Foundation of Korea (NRF), funded by the Ministry of Education (RS-2021-NR060141).

Conflicts of Interest: The authors declare no conflicts of interest.

Abbreviations

The following abbreviations are used in this manuscript:

HEA	High-Entropy Alloy
SPS	Spark Plasma Sintering
PM	Powder Metallurgy
HT	Heat Treatment
XRD	X-ray Diffraction
SEM	Scanning Electron Microscopy
EDS	Energy-Dispersive Spectroscopy
FCC	Face-Centered Cubic
BCC	Body-Centered Cubic
HV	Vickers Hardness
ΔHmix	Mixing Enthalpy
ΔSmix	Mixing Entropy
VEC	Valence Electron Concentration
MPa	Megapascal
at.%	Atomic Percent
wt.%	Weight Percent

References

1. Cai, G.; Huang, Y.; Qing, Y.; Misra, R.D.K. Effects of Y and Hf addition on soft magnetic property and ductility improvement of Fe–6.9 wt% Si alloy. *J. Mater. Res. Technol.* **2025**, *37*, 1362–1378. [CrossRef]
2. Han, C.; Huang, J.; Ye, X.; Liu, B.; Dong, Z.; Yang, Y.; Gao, J.; Yang, K.; Chen, G. Microstructure evolution and ductility improvement of additively manufactured biodegradable zinc–magnesium alloys via annealing. *Int. J. Bioprinting* **2024**, *10*, 3034. [CrossRef]
3. Hong, Y.; Huang, S.Q.; Chen, W.L.; Lin, S.S.; Fan, T.W.; Wu, Y.Z.; Xu, W.; Gong, D.Z.; Yan, J.; Deng, B. Solid particle erosion behavior and failure mechanism of medium-entropy AlCrTiSiN coatings. *Tribol. Int.* **2026**, *218*, 111775. [CrossRef]
4. Li, X.; Zhao, Y.; Peng, Y.; Shi, S.; Liu, K.; Xu, G.; Lei, Y.; Lu, N.; Wang, H.; Lin, X. Bulk single-crystal-like IN738 alloy fabricated using laser powder bed fusion by controlling the thermal flow. *Mater. Res. Lett.* **2025**, *13*, 1072–1079. [CrossRef]

5. Chen, B.; Wang, S.; Li, W.; Zheng, H.; Lu, Y.; Qi, Z.; Wang, Q.; Zhang, S.; Yao, J.; Li, Y. Investigation on the atomization mechanism of alloy powder by dual-gas nozzle and the powder defects formation. *Powder Technol.* **2026**, *469*, 121768. [CrossRef]
6. Peng, J.; Xie, S.; Xia, J.; Wang, X.; Ni, Z.; Wang, P.; Chen, N. Investigation of Process and Properties of Cu-Mn-Al Alloy Cladding Deposited on 27SiMn Steel via Cold Metal Transfer. *Crystals* **2025**, *15*, 858. [CrossRef]
7. Yuan, Z.; Lu, Y.; Tu, Y.; Yuan, T.; Wang, X.; Ni, Z.; Han, P.; Liu, F.; Huo, W. Microstructure and corrosion behavior of Al-Cu intermetallics in laminated sheets. *Intermetallics* **2025**, *187*, 109022. [CrossRef]
8. Li, Z.; Gou, J.; Gao, J.; Zhu, J.; Kou, W.; Wang, J. Microstructural evolution and corrosion resistance of additively manu-factured Ti–6Al–4V alloy annular shaped components using multistage heat treatment. *Mater. Chem. Phys.* **2025**, *346*, 131414. [CrossRef]
9. Wang, Y.; Peng, Y.; Qin, W.; Zhu, L.; Xie, Y.; Liu, B.; Wang, X.; Zhang, G.; Xu, D. Mechanism of amorphous SiO_2 grain boundary modulation to inhibit abnormal grain growth and high-temperature strengthening of 3YSZ ceramic fibers. *J. Eur. Ceram. Soc.* **2026**, *46*, 118128. [CrossRef]
10. Fu, Y.; Mehr, V.Y.; Toroghinejad, M.R.; Chen, X.; Jie, J.; Zhu, S. Twinning and stacking fault-induced precipitation in an aluminum alloy. *J. Mater. Res. Technol.* **2025**, *34*, 2127–2132. [CrossRef]
11. Mao, F.; Guo, J.L.; Liu, S.H.; Zhang, L.; Guo, A.; Chen, C.; Chen, Z.; Li, J.; Wang, T.; Wei, S. Spheroidization mechanism of primary silicon in hypereutectic Al–Si alloys with Eu addition. *Rare Met.* **2025**, *44*, 7940–7955. [CrossRef]
12. Zhao, Y.C.; Ma, H.W.; Sun, J.D.; Luo, J.; Su, Y.; Feng, L.; Liu, T.; Zhan, F.; Yu, Z.; Yang, T.; et al. A Xanthium sibiricum biomimetic Fe-based medium-entropy alloy with significant antibacterial and mechanical behaviors. *Rare Met.* **2025**, *44*, 4913–4935. [CrossRef]
13. Ma, P.; Yang, H.; Zhang, Z.Y.; Xie, X.C.; Yang, P.; Konda-Gokuldoss, P.; Zhang, H.; Jia, Y.D. Microstructure and mechanical properties of additively manufactured FeCoCrMnNi high-entropy alloy composite after aging. *J. Central South Univ.* **2025**, *32*, 1167–1178. [CrossRef]
14. Wang, W.; Wu, L.; Li, Z.; Mu, W.; Wang, F.; Zhang, W.; Wang, N.; Weng, Z. Passivation, layered surface high-temperature oxidation, and mechanical behaviors in Al-doped cobalt-based dual-phase multi-principal element alloys. *Appl. Surf. Sci.* **2026**, *719*, 164930. [CrossRef]
15. Ren, K.; Ma, R.; Wang, Z.; Qin, S.; Chen, R.; Ma, X.; Ma, P.; Li, S.; Xie, Z.; Yao, X.; et al. Grain size dependence of TiZrNbV spallation and impact-energy-release behavior. *Int. J. Mech. Sci.* **2025**, *293*, 110164. [CrossRef]
16. Nagarjuna, C.; Dewangan, S.K.; Rao, K.R.; Mohan, M.; Lee, H.; Song, E.; Ahn, B. Strengthening of mechanical and tribological properties in CrFeCuMnNi high entropy alloy through dispersion of TiO_2 reinforcement via powder metallurgy processes. *Ceram. Int.* **2024**, *50*, 53059–53072. [CrossRef]
17. Ganesan, D.; Sellamuthu, P.; Prashanth, K.G. Vacuum Hot Pressing of Oxide Dispersion Strengthened Ferritic Stainless Steels: Effect of Al Addition on the Microstructure and Properties. *J. Manuf. Mater. Process.* **2020**, *4*, 93. [CrossRef]
18. Dewangan, S.K. *Studies on Microstructure, Mechanical and High-Temperature Oxidation Behaviour of Tungsten Containing High Entropy Alloys*; Indian Institute of Technology Indore: Indore, India, 2021.
19. Liu, Y.; Shao, L.; Zhang, S.; Hu, L.; Wu, Y.; Liu, C.; Huang, Y.; Le, P.; Li, W.; Xue, N.; et al. Effect of chemical composition and heat treatment on the microstructure and performance of Ag-based alloy wires. *Mater. Des.* **2025**, *258*, 114728. [CrossRef]
20. Xie, B.; Ning, Y.; Luo, Y.; Wang, Z.; Shi, B.; Zhan, M.; Fu, M. Achieving serrated grain boundaries within gradient microstructures of nickel-based superalloys for dual-property turbine disks in aeroengines. *Chin. J. Aeronaut.* **2026**, *39*, 103910. [CrossRef]
21. Shen, C.; Wang, C.; Wei, X.; Li, Y.; van der Zwaag, S.; Xu, W. Physical metallurgy-guided machine learning and artificial intelligent design of ultrahigh-strength stainless steel. *Acta Mater.* **2019**, *179*, 201–214. [CrossRef]
22. Jiang, X.P.; Yu, W.; Wei, Y.; Wu, H.; Ding, J.; Hu, C.; Liu, X.; Feng, J.; Chong, X. Tailoring precipitation-strengthening in Ir-based ternary alloys: A first-principles approach to L12 phase engineering. *Rare Met.* **2025**, *44*, 9036–9052. [CrossRef]
23. Peng, J.; Xie, S.; Chen, T.; Wang, X.; Yu, X.; Yang, L.; Ni, Z.; Ling, Z.; Yuan, Z.; Shi, J.; et al. Numerical Simulation and Process Optimization of Laser Welding in 6056 Aluminum Alloy T-Joints. *Crystals* **2024**, *15*, 35. [CrossRef]
24. Shen, L.; Li, Y.; Zhang, W.; Zhang, S.; Ma, S.; Peng, F.; Wu, Z. Machine learning-assisted design of strong and ductile BCC high-entropy alloys. *Mater. Res. Lett.* **2025**, *13*, 1260–1268. [CrossRef]
25. Peng, J.; Xie, S.; Xia, J.; Wang, X.; Ni, Z.; Wang, P.; Chen, N. Effect of the Activator $B(OCH_3)_3$ on the Microstructure and Mechanical Properties of Cu-Mn-Al Alloy Coating via CMT Cladding. *Crystals* **2025**, *15*, 881. [CrossRef]
26. Li, X.; Zhang, L.; Li, Y.; Zhao, Y.; Guo, Z.; Wang, H.; Liu, K.; Bai, P.; Liu, B.; Tang, H.; et al. Advances in additive manufacturing of cemented carbides: From powder production to mechanical properties and future challenges. *Curr. Opin. Solid State Mater. Sci.* **2025**, *38*, 101238. [CrossRef]
27. Rohila, S.; Mane, R.B.; Ummethala, G.; Panigrahi, B.B. Nearly full-density pressureless sintering of AlCoCrFeNi-based high-entropy alloy powders. *J. Mater. Res.* **2019**, *34*, 777–786. [CrossRef]
28. Rao, K.R.; Dewangan, S.K.; Seikh, A.H.; Sinha, S.K.; Ahn, B. Microstructure and Mechanical Characteristics of AlCoCrFeNi-Based ODS High-Entropy Alloys Consolidated by Vacuum Hot Pressing. *Met. Mater. Int.* **2024**, *30*, 726–734. [CrossRef]
29. Yu, Y.; Wang, J.; Li, J.; Kou, H.; Liu, W. Characterization of BCC phases in AlCoCrFeNiTix high entropy alloys. *Mater. Lett.* **2015**, *138*, 78–80. [CrossRef]

30. Xiang, C.; Zhang, Z.M.; Fu, H.M.; Han, E.-H.; Zhang, H.; Wang, J. Microstructure and corrosion behavior of $AlCoCrFeNiSi_{0.1}$ high-entropy alloy. *Intermetallics* **2019**, *114*, 106599. [CrossRef]
31. Zhu, J.; Meng, J.; Liang, J. Microstructure and mechanical properties of multi-principal component $AlCoCrFeNiCu_x$ alloy. *Rare Met.* **2016**, *35*, 385–389. [CrossRef]
32. Dewangan, S.K.; Kumar, D.; Samal, S.; Kumar, V. Microstructure and Mechanical Properties of Nanocrystalline $AlCrFeMnNiW_x$ (x = 0, 0.05, 0.1, 0.5) High-Entropy Alloys Prepared by Powder Metallurgy Route. *J. Mater. Eng. Perform.* **2021**, *30*, 4421–4431. [CrossRef]
33. Guo, S.; Ng, C.; Lu, J.; Liu, C.T. Effect of valence electron concentration on stability of fcc or bcc phase in high entropy alloys. *J. Appl. Phys.* **2011**, *109*, 103505. [CrossRef]
34. Nagarjuna, C.; Dewangan, S.K.; Lee, H.; Madavali, B.; Ahn, B. Effect of Si alloying on the structural, thermal expansion, and magnetic properties of FeCoNiAlSix high-entropy alloys. *J. Mater. Sci.* **2024**, *59*, 4281–4292. [CrossRef]
35. Dewangan, S.K.; Nagarjuna, C.; Lee, H.; Sharma, A.; Ahn, B. Surface morphology transformation and densification behaviour of conventionally sintered AlFeCoNiSi high entropy alloys. *Powder Met.* **2023**, *66*, 650–661. [CrossRef]

Disclaimer/Publisher's Note: The statements, opinions and data contained in all publications are solely those of the individual author(s) and contributor(s) and not of MDPI and/or the editor(s). MDPI and/or the editor(s) disclaim responsibility for any injury to people or property resulting from any ideas, methods, instructions or products referred to in the content.